JMEPEG (2010) 19:885–893
DOI: 10.1007/s11665-009-9540-5

1059-9495/$19.00

Microstructure-Mechanical Property Relationships for a Fe/Mn/Cr Rock Bolt Reinforcing Steel

B.K. Panigrahi

(Submitted December 7, 2008; in revised form July 19, 2009)

The influence of low chromium additions to a 0.25C-1.5Mn semikilled steel on microstructure, and tensile and impact behaviors of high strength rock bolt reinforcing bars has been investigated. Although chromium imparted adequate tensile properties at ambient temperature (yield stress: 624 MPa; ultimate tensile stress: 819 MPa; elongation: 12.5%) by forming transformation products such as tempered martensite, lower and upper bainite, and small amounts of acicular ferrite, it increased the ductile-to-brittle transition temperature due to coarser upper bainite in the core region of bar having larger unit crack paths. The synthesized steel is considered to be effective in realizing the desired tensile properties, and suitable for application in rock bolt, as well as other reinforced concrete structures.

Keywords mechanical properties, microstructure, rock bolt reinforcing bar, thin foil electron microscopy

1. Introduction

There has been a surge in demand for high strength reinforcing steel bar, and several hundred thousands tons are used in construction projects every year. The reinforcing steels have a minimum yield strength of 420 to 600 MPa. High-strength steels are intended for construction projects such as multistory buildings, highways, and tunnels. Another major application of this steel is rock bolt (Ref 1). Rock bolts are used to reinforce roofs of tunnels, and underground mines, support walls, and are characterized by high yield stress, ultimate tensile stress, and moderate elongation. One way of manufacturing the high strength rock bolt is by thermomechanical treatment (TMT) wherein the material during hot rolling passes through an in-line quenching unit to produce optimum microstructure and mechanical properties. The sequence of processing of rock bolt is shown in Fig. 1. Significant advances have been made in the previous two decades in our understanding of alloy design, microstructure, and mechanical properties of TMT reinforcing steel (Ref 2-7). However, these advances are mostly for reinforcing steel having a minimum yield strength of up to about 500 MPa. It has been estimated that a saving in steel consumption to the tune of 36% can be achieved by replacing 500 MPa yield strength steel with a 600 MPa yield strength steel (Ref 8). Previous investigators (Ref 8-10) have discussed the effects of Mn, Cr, Ni, Mo, B, Nb, V, and Ti alloying to achieve the high strength and other mechanical properties of reinforcing steel. However, these studies focused on steels with 0.2-2.4% Si and 0.6-1.7% Cr. In order to minimize the alloy cost and meet the growing demand for rock bolt steel by mining and construction industry, a study has been made with cheaper C-Mn-Cr semikilled steel which has not been evaluated for suitability as rock bolt, and for other reinforced concrete structures.

B.K. Panigrahi, Padmanava College of Engineering, Sector 4, Rourkela 769 002, India. Contact e-mails: bimal.panigrahi@gmail.com and bimal.panigrahi@yahoo.com.

2. Materials and Methods

The steel for TMT rebar was made in a 250T twin-hearth furnace and cast into ingots each weighing 9 tons. The ingots were soaked at 1300-1350 °C for 4 h, rolled to blooms of size 325 × 325 mm, and then to billets of size 100 × 100 mm. The billets were reheated at 1150-1200 °C in a furnace, soaked for about 2 h, and subsequently rolled in multiple rolling stands (roughing, intermediate, and finishing stands). From the finishing stand at a finishing rolling temperature (FRT) of 950-1000 °C, the bar passed through an in-line quenching unit where the bar was quenched by pressurized water at about 250 °C/s till the surface temperature of the bar dropped to ~200 °C while the core remains in austenitic state. On emergence from the cooling unit, the temperature of the bar equalizes (equalization temperature) due to transfer of heat from the core to the rim. Thereafter, the bar cooled down to the ambient temperature in natural air on the bar cooling bay. The equalization temperature (ET) of the bar was 540 ± 10 °C. The schematic of the processing schedule is shown in Fig. 2.

For macrophotography, and light and scanning electron microscopy, transverse specimens were ground and polished with successively finer abrasives using water. The final polishing was done with alumina paste. The polished specimens were etched in 2% nital and examined using a scanning electron microscope (JEOL JSM-840A) operating at 20 keV. A 5 mm long sample of the bar was cut and soaked at 950 ± 5 °C for 15 min and quenched in brine solution. The sample was cut into two pieces. One of the cut surfaces was polished and etched as above to examine as-quenched microstructure approximately 2-5 mm from the surface of bar.

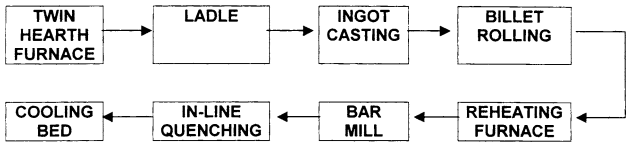

Fig. 1 Sequence of processing of high-strength rock bolt

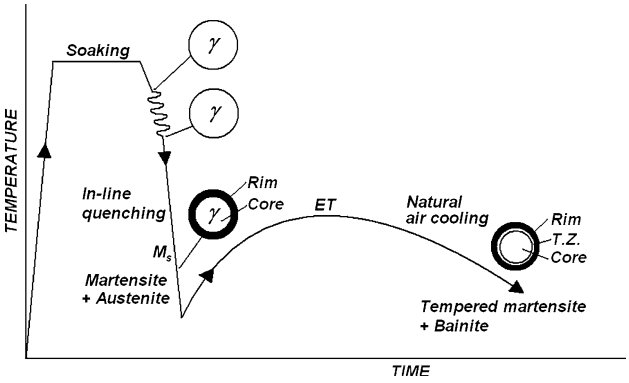

Fig. 2 Schematic of processing schedule of high-strength rock bolt

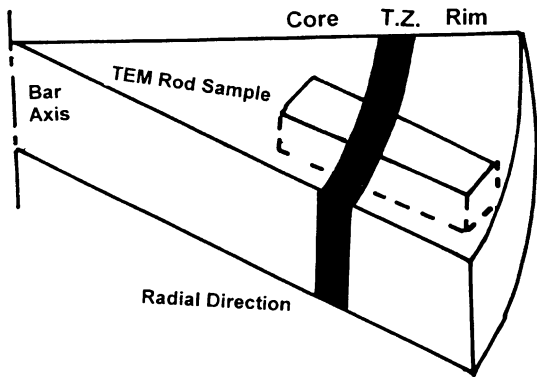

Fig. 3 Schematic showing location of TEM samples

The thin foils for transmission electron microscopy were prepared from rod sample ($4 \times 4 \times 10$ mm) machined to include rim, transition zone, and core of the bar as shown in Fig. 3. Wafers ~0.5 mm thick were cut from the rod immersed in a coolant by a diamond disc cutter from which 3 mm diameter foils were punched. The punched specimens were mechanically ground to a thickness below 0.1 mm, electropolished in a solution of 5% perchloric acid 95% glacial acetic acid at 20 °C and observed with an electron microscope (JEOL JEM 4000EX) at 150 keV.

Tensile testing of the hot-rolled rebar at ambient temperature (RT = +30 °C) was carried out without surface machining (Fig. 4a). Tensile testing was also carried out using round tensile specimens machined as per ASTM A 370 standard from the core (Fig. 4b) of the rebar. In all cases, duplicate tensile specimens were used. Tensile test for the unmachined full-diameter bar was performed in a universal testing machine at a crosshead speed of 10 mm/min at ambient temperature.

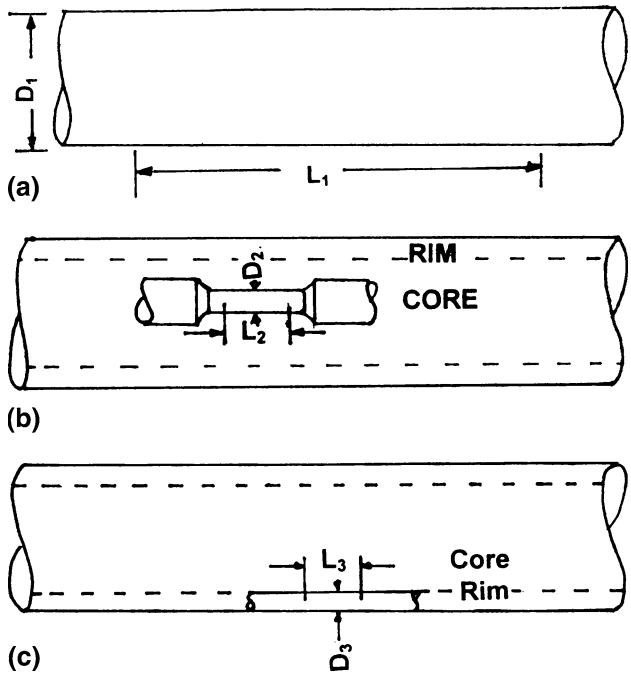

Fig. 4 Tensile specimen of unmachined hot-rolled bar (a) and location of tensile specimens from core of rebar (b), and from the rim of rebar (c) [gauge length: L_1, L_2, L_3; gauge diameter: D_1, D_2, D_3; where L_1 = 160 mm, D_1 = 32 mm; L_2 = 25 mm, D_2 = 6.25 mm; L_3 = 20 mm, D_3 = 4 mm]

The elongation was measured manually for a gauge length (L_1) of $5.65\sqrt{A}$, where A is the cross-sectional area of the bar. The total length of the specimen was 700 mm. Specimens prepared from the core region of rebar were tested at a crosshead speed of 2 mm/min. The elongation was measured for a gauge length (L_2) of 25 mm (L_2:D_2 = 4) for core specimens with extensometer attached to the specimens. Due to extremely high hardness, standard tensile specimen (2.5 mm gauge diameter) could not be prepared from the rim region. In order to measure the tensile properties, a 4 mm diameter rod, 70 mm long was machined from the rim (Fig. 4c) and tested. After the tensile test at crosshead speed of 2 mm/min, the elongation was measured manually for a gauge length of 20 mm. Vickers hardness of rim, transition zone, and core was measured with a load of 30 kg. Ten indentations were made in each zone for average hardness of respective zones. The Charpy V-notch impact toughness was evaluated using sub-size ($5 \times 10 \times 55$ mm) longitudinal specimens machined from the location shown in Fig. 5 and tested at RT, 0, −20, and −40 °C as per ASTM E 23 standard. The V-notch was cut in the rim of TMT bar so that about 1 mm of rim remained intact ahead of the notch. The ductile-to-brittle transition temperature (DBTT) was determined from the 50% of the maximum absorbed energy value. The DBTT calculated by this method gives same result as DBTT calculated from 50% of the cleavage fracture area (Ref 11). The fracture surface of broken Charpy specimens was studied by a scanning electron microscope (JEOL JSM-840A) operating at 20 keV using the secondary electron imaging mode. The tensile fracture surface of the rim specimen was studied by scanning electron microscope as mentioned above; energy dispersive spectroscopy (EDS) of inclusions of broken tensile specimens was carried out at 10 keV.

3. Results and Discussion

3.1 Chemical Composition

The alloy design for high-strength TMT rebar is based on the requirement of strength, ductility, and weldability. The chemical composition of the semikilled Mn-Cr steel obtained from optical emission spectroscopy is given in Table 1. Mn and Cr increase the hardenability of Fe-C alloys and can lead to bainitic microstructure in the core of TMT bar after processing since Cr reduces the diffusion coefficient of carbon in ferrite (Ref 12). Both C and Cr favor formation of retained austenite in as quenched steel (Ref 13). Although Si increases the hardenability, retards cementite formation and its coarsening, and is a solid solution strengthener, it was kept below 0.10%, mainly due to economic considerations. The martensite start (M_s) temperature for this steel, estimated from the following empirical equation (Ref 14), is 378 °C:

$$M_s\ (^\circ\mathrm{C}) = 561 - 474(\%\mathrm{C}) - 17(\%\mathrm{Cr}) - 33(\%\mathrm{Mn}) - 21(\%\mathrm{Mo,\ Si,\ W}) - 17(\%\mathrm{Ni}) \quad \text{(Eq 1)}$$

The kinetics of bainite reaction extends to a temperature of about 100-300 °C below the eutectoid temperature. Higher the addition of alloying elements, lower is the bainite start temperature (Ref 15, 16).

3.2 Macro and Microstructure

Figure 6 shows the macrostructure of rock bolt. There is a darker rim surrounding a transition zone, and core with approximate area of 36, 13.3, and 50.7% respectively. A and B are the longitudinal ribs. The core region appears non-uniformly etched due to segregation of alloying elements during ingot casting that could not be homogenized at the later stages of reheating and soaking. It is well known that as-quenched lath martensite consists of lath, sub-block, block, packet, and prior austenite grains with numerous transformation-induced mobile dislocations (Ref 17). When the bar enters the cooling unit at high FRT, it has a less coarse austenite grain size, produced due to static/(dynamic) recrystallization in the successive rolling stands. During quenching as soon as the first martensite is formed from the supersaturated solid solution, carbon atoms have enough time to be redistributed so as to cluster at dislocations, and other lattice defects, which eventually grow to carbides (Ref 18). This process is referred as self-tempering, or auto tempering, and may continue up to 200 °C, so that the approximate range of self-tempering process is about 175 °C. Due to transfer of heat from the core, the temperature of rim rises, and finally a steady bar temperature (ET) is attained. The rim is slightly tempered at this lower ET, and this process continues till the bar temperature drops to about 200 °C. The light (a) and scanning electron (b) micrographs of as-quenched specimen are shown in Fig. 7. The presence of a few particles (C) in the martensite crystals were observed in as-quenched specimen (Fig. 7b). Due to their extremely small size, they could not be analyzed in scanning electron microscope. However, it appears that they are carbide particles. The light and scanning electron micrographs of rim, transition zone, and core are shown in Fig. 8. The rim exhibited a slightly tempered martensite structure (Fig. 8a), the transition zone showed a relatively finer bainitic structure with small amount of pearlite (Fig. 8b), and core showed a coarser bainitic structure with pearlite (Fig. 8c). The average Vickers hardness values of rim, transition zone, and core were 306, 243, and 231 VHN, respectively, which correspond to UTS of approximately 1040, 826, and 785 MPa, respectively (Ref 19) according to the relationship UTS = 3.4 (Brinell hardness number), since at lower hardness level Brinell hardness number is close to the Vickers hardness number. The hardness data are consistent with earlier investigations (Ref 16).

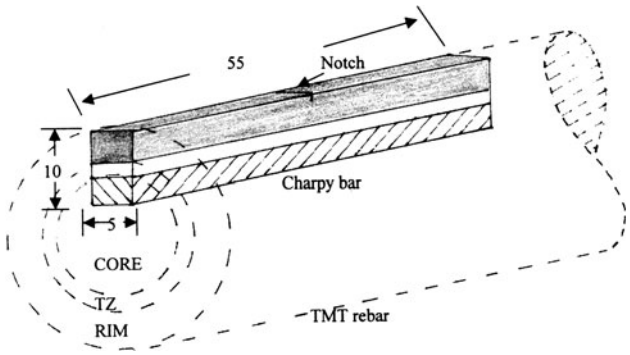

Fig. 5 Location of Charpy V-notch specimen in the reinforcing bar

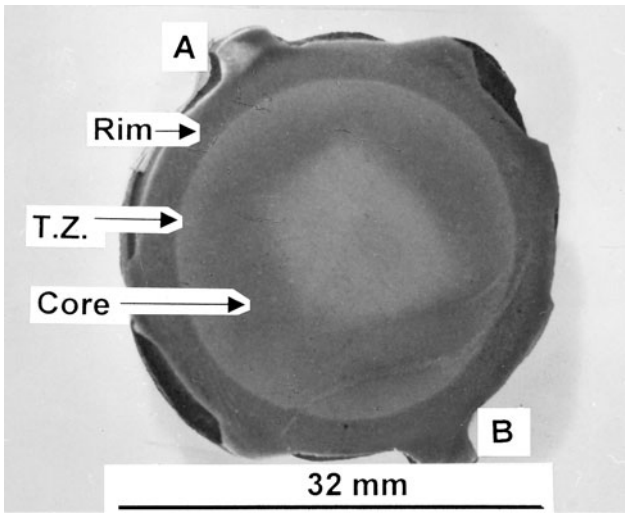

Fig. 6 Macrostructure of rock bolt bar

Table 1 Chemical composition of TMT rebar (wt.%)

Heat number		C	Mn	Si	S	P	Cr	Al	N
39585	Heat analysis	0.25	1.42	0.056	0.024	0.024	0.540	nd	nd
	Product analysis	0.27	1.47	0.060	0.031	0.029	0.570	0.004	0.0075

nd, not determined

Transmission electron micrograph (TEM) of rim region are shown in Fig. 9. Figure 9 shows lath carbides most of which formed during brief exposure at the equalization temperature; these carbides are mainly Fe_3C, and not $(Fe, Mn, Cr)_3C$, since at the low temperature of bainitic reaction, the substitutional solute atoms are literally immobile in austenite and ferrite to form alloy carbides. TEM of transition zone, which experiences a cooling rate during in-line quenching intermediate to that of rim and core, revealed a lower bainitic structure with intralath carbides arranged in a single crystallographic orientation (Fig. 10). This observation is consistent with previous reports (Ref 20, 21).

Figure 11 shows the TEM micrographs of core region, which experiences relatively slow cooling during quenching, an upper bainite structure having small subunits (Fig. 11a) with interlath and intralath precipitation of carbide particles at dislocations. These carbide particles in upper bainite are exclusively cementite. The intralath carbide particles aligned in the bainitic ferrite laths were thought to have formed previously on the subunit edges. The coalescence of the subunits makes the precipitate

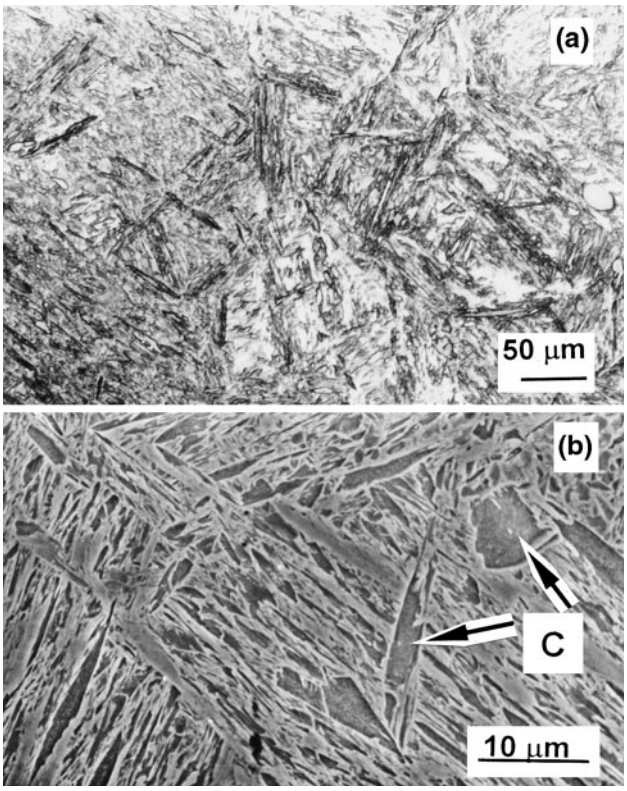

Fig. 7 As-quenched (a) light and (b) scanning electron micrographs of bar

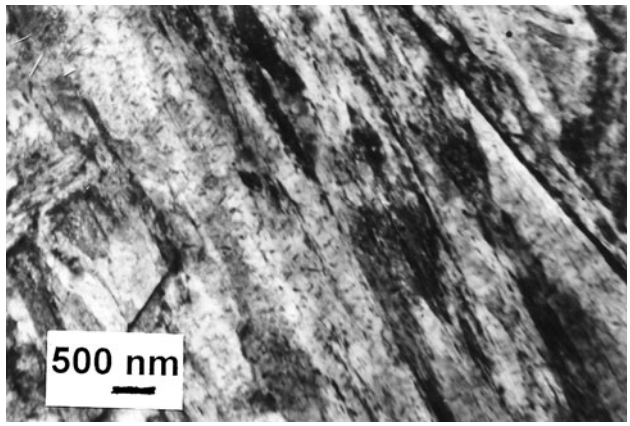

Fig. 9 Transmission electron micrograph of rim

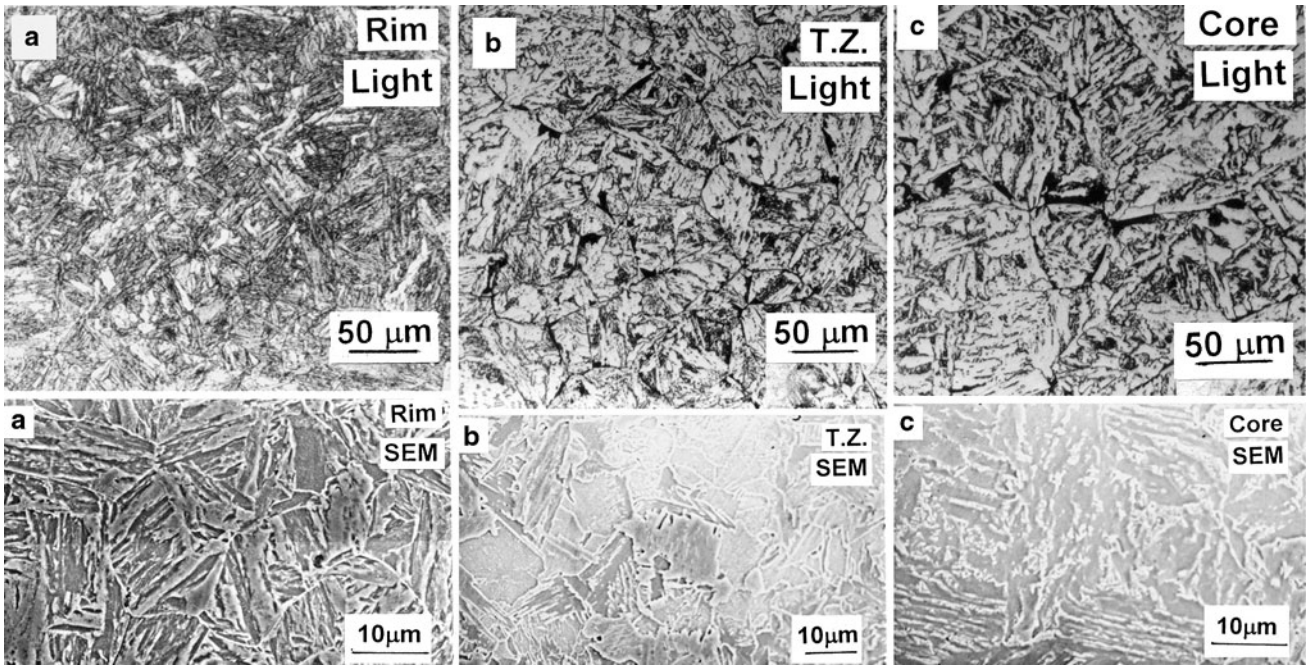

Fig. 8 Light and scanning electron micrographs (SEM) of (a) rim, (b) transition zone, and (c) core

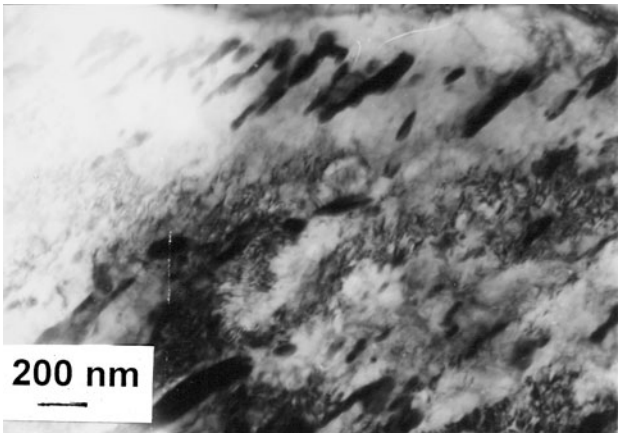

Fig. 10 Transmission electron micrograph of transition zone

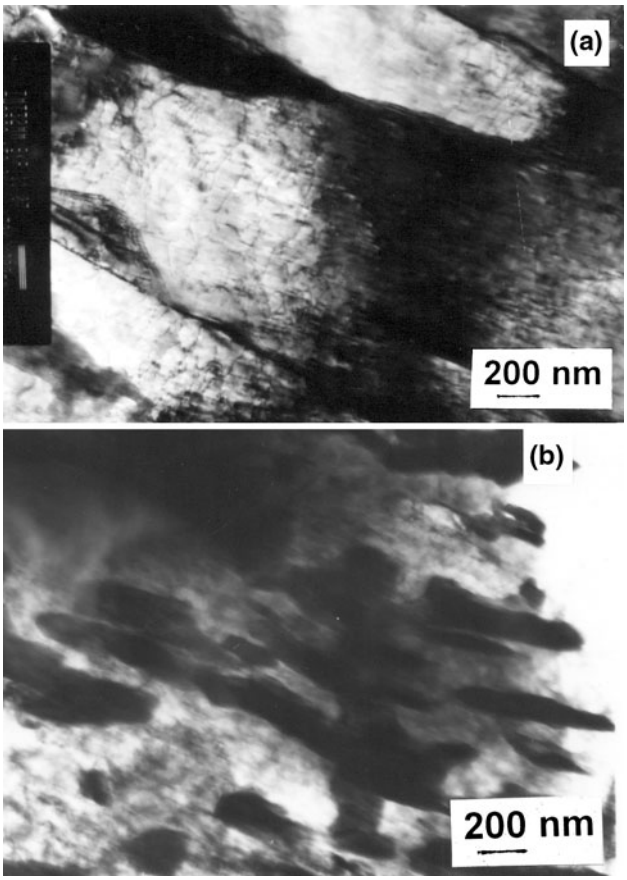

Fig. 11 Transmission electron micrographs of core

particles to appear as intralath carbide (Ref 16). The interlath carbides are formed by decomposition of carbon-enriched austenite entrapped between bainitic ferrite laths. The carbides often appeared as irregular ribbons (Fig. 11b). A similar morphology of carbide was reported in a Fe-0.2%C-2%Cr-1%V alloy steels in which the carbides are alloy carbide equivalent of pearlite (Ref 22). When the carbon content in the steel is in excess of that required to combine with alloying elements, pearlite begins to form during the $\gamma \rightarrow \alpha +$ carbide reaction at a stage when the residual austenite is enriched to a critical carbon level (Ref 22).

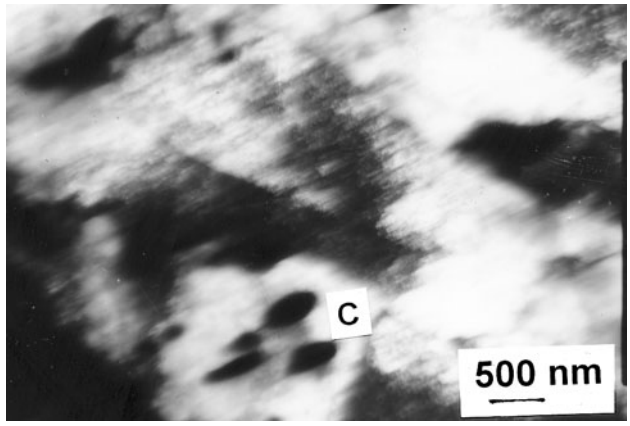

Fig. 12 Transmission electron micrograph of core showing acicular ferrite

Table 2 Tensile properties of as-hot-rolled TMT bar, core, and rim at ambient temperature

	Experimental steel		
	Yield/0.2% proof stress, MPa	Ultimate tensile stress, MPa	Elongation, %
As-hot-rolled bar	624	819	12.5
Core	543	667	19.1
Rim	nd	991	5.8
As specified by ASTM F 432-04 Grade 75	517	688	8

nd, not determined

Figure 12 shows a high magnification TEM view of core in which spherical to lenticular intralath carbides (C) associated with acicular ferrite are observed. This is consistent with the observation of Bramfitt and Speer (Ref 23). The inhomogeneity produced by ingot casting operation led to regions enriched and depleted in C, Mn, and Cr, and produced microstructure having different constituents after the transformation of austenite.

3.3 Yield and Ultimate Tensile Stress at RT

The specified and actual yield stress, and ultimate tensile stress of rebar, are given in Table 2. The yield and ultimate tensile stress of as-hot rolled full diameter bar were 624 and 819 MPa, respectively, which conform to ASTM F 432 Gr. 75 steel. Factors that can contribute to the yield strength in this transformation strengthened steel are Mn in solid solution, lath size, density of carbide particles, and dislocation density of the slightly tempered martensite, and bainitic ferrite (Ref 24, 25). Untransformed retained austenite decreases the yield strength since austenite is a ductile phase. The yield and ultimate tensile stress of bainitic core region were 543 and 667 MPa, respectively. The yielding behavior of core was continuous (Fig. 13) due to bainite structure with high density of mobile dislocations. The predominantly coarser upper bainite structure of the core produced the high strength. The ultimate tensile stress and elongation of the rim were 991 MPa and 5.8%, respectively.

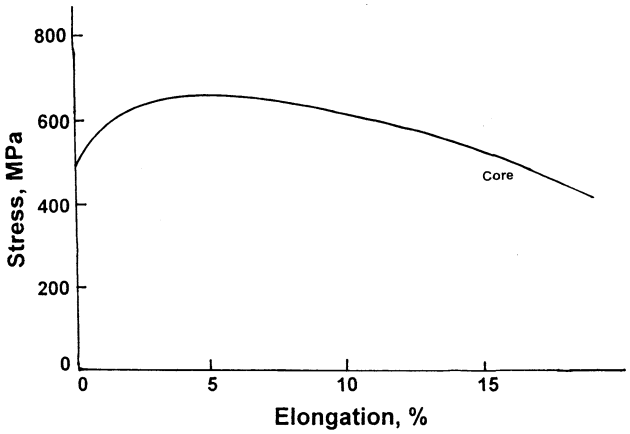

Fig. 13 Engineering stress-strain curve of longitudinal specimen of core at ambient temperature

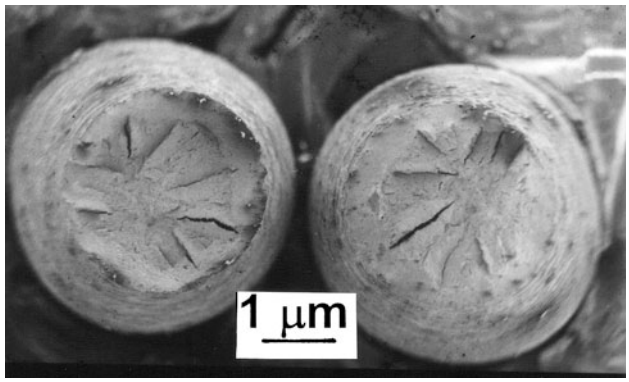

Fig. 14 Scanning electron micrographs of broken tensile specimen from the rim of TMT bar showing cup-and-cone fracture with delaminations

The ultimate tensile stress of rim as estimated from the hardness value was quite similar. The limitation of test specimens did not permit calculation of the 0.2% offset stress of rim which would be quite high due to slightly tempered martensite structure with a high density of mobile dislocations. A cup-and-cone type fracture was observed in as-hot-rolled bar, core, and rim specimens indicating a ductile mode of fracture. The typical fractured surface of rim exhibits delaminations normal to the tensile axis (Fig. 14). Similar features were observed in the fractographs of as-hot-rolled bar and core specimens. A closer look at fracture mode showed that it was a case of a ductile fracture with dimples of relatively finer size (Fig. 15), though the delamination part is a cleavage fracture. Since the size of dimples exhibits a direct proportionality with strength and ductility, finer dimples indicate higher strength and ductility of the rim. These dimples have irregular inclusions of different sizes within. In the tensile test, voids form prior to necking and coalesce (Fig. 16a) to form a main line crack. Second phase particles act as sites for void nucleation. The energy dispersive spectrometer (EDS) results of particles (Fig. 16b) within few dimples could not identify the nature of these particles and was biased toward the matrix elements, namely Fe, Mn, and Cr. However, it appears that the particles are iron oxide and manganese oxide. The fractograph of shear lip from the cup part of tensile specimen displays a parabolic-shaped fracture

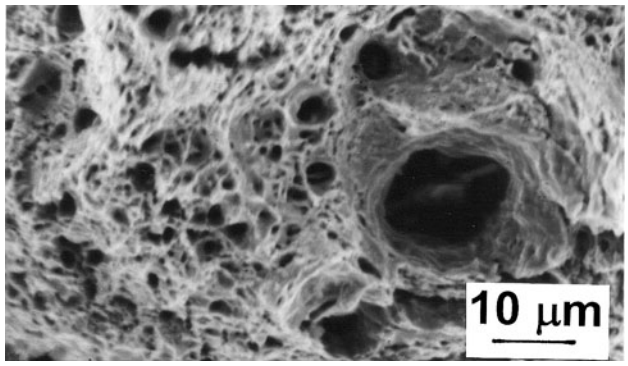

Fig. 15 Scanning electron micrograph of a dimpled region in between the delaminations in the cup

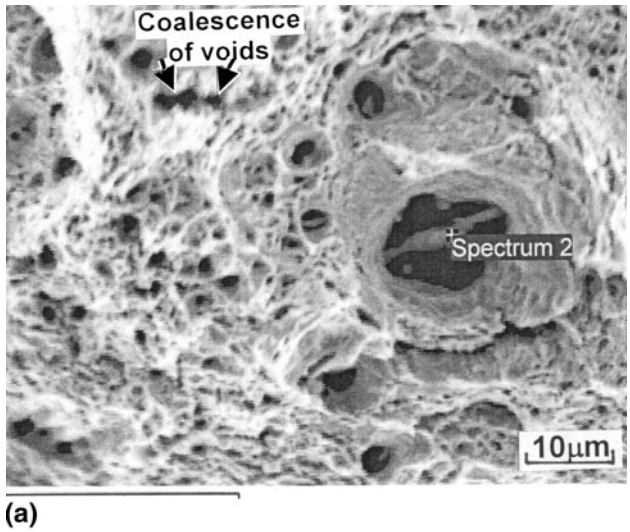

Fig. 16 Scanning electron micrograph showing (a) nucleation of voids and coalescence in the cup and (b) EDS spectrum

surface with dimples and micro-delaminations (Fig. 17), which is a characteristic feature of shear fracture. Since the delaminations were concentrated adjacent to the shear lips at the periphery of the fracture surface (Fig. 14), it follows that a ductile crack formed first at the center of the specimen, where the transverse stress is higher. The delaminations are formed after this due to transverse tensile stresses in the neck of the tensile specimen, followed by rupture of the ligaments between

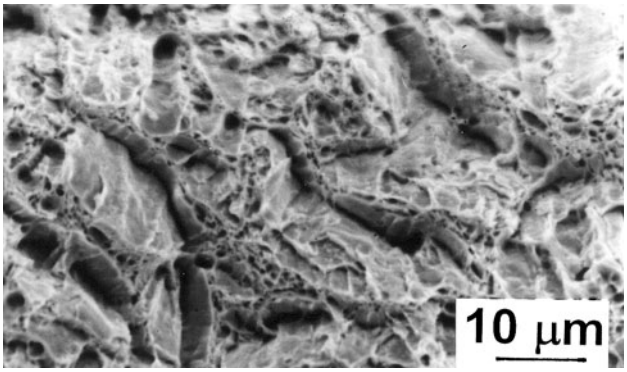

Fig. 17 Scanning electron micrograph of parabolic-shaped fracture surface with microdelaminations in the shear lip of the cup

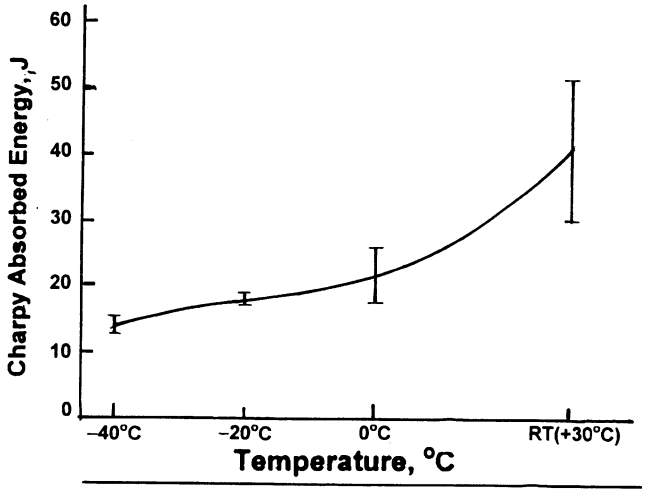

Fig. 18 Impact transition curve from the half-size longitudinal specimens

the delaminations, and the final shear fracture. Similar fractographs have been observed in the tensile fracture of high-strength steel plate (Ref 26).

3.4 Elongation

The total elongation of the hot-rolled TMT rebar was 12.5%. The ASTM standard F 432 Gr. 75 specifies a minimum elongation of 8% for rock bolt. In view of mixed microstructures in the TMT rebar, a multitude of factors influences the total elongation. These are amount of microstructural constituents, size, volume fraction, and morphology of carbide, inclusions, and dislocation density. The presence of predominantly bainitic microstructure in the core of TMT rebar resulted in high flow stresses (Fig. 13). The inclusion particles that are present in the core can act as void sources (Fig. 15). These voids can link-up to a main line crack. Voids can also nucleate at grain boundary, and interlath carbides, linking up to form a least difficult path for propagation of crack through the matrix which also causes lower ductility (Ref 27, 28).

3.5 Charpy Impact Toughness

The impact transition curve from the half-size longitudinal specimens is shown in Fig. 18. The Charpy energy of rim at 0 °C is 21 J. The DBTT based on 50% of maximum absorbed energy criterion (Ref 11) is −2 °C. The relatively moderate absorbed energy and higher DBTT could be due to chromium which favors transformation to upper bainite in the core. The coarser bainitic structure ahead of the notch has larger unit crack path in it. A crack nucleates within a unit, propagates easily, thereby decreasing the absorbed energy and increasing the DBTT. The carbide particles between platelets of upper bainite in core can increase the DBTT, because constraint to slip extension by carbides is likely to result in strain localization. In order to accommodate the strain localization, multiple slips are activated and dislocations on different slip systems interact and favor initiation of microcracks (Ref 29) and their propagation in upper bainite. In view of this, Cr

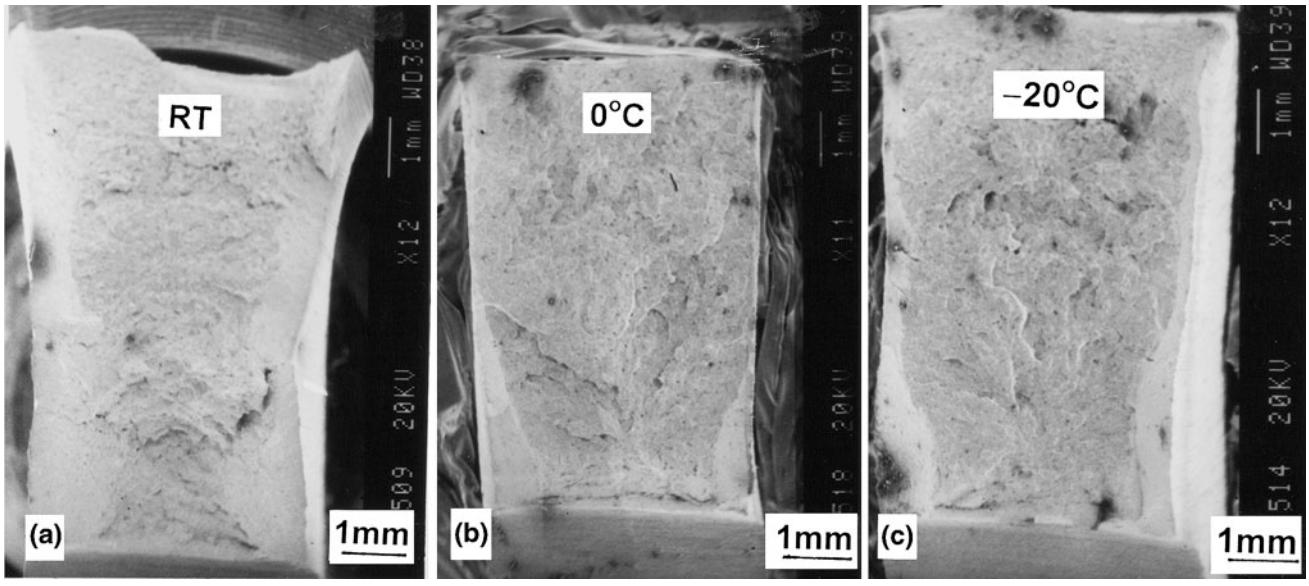

Fig. 19 Low magnification scanning electron fractographs of broken Charpy specimens at (a) RT, (b) 0 °C, and (c) −20 °C

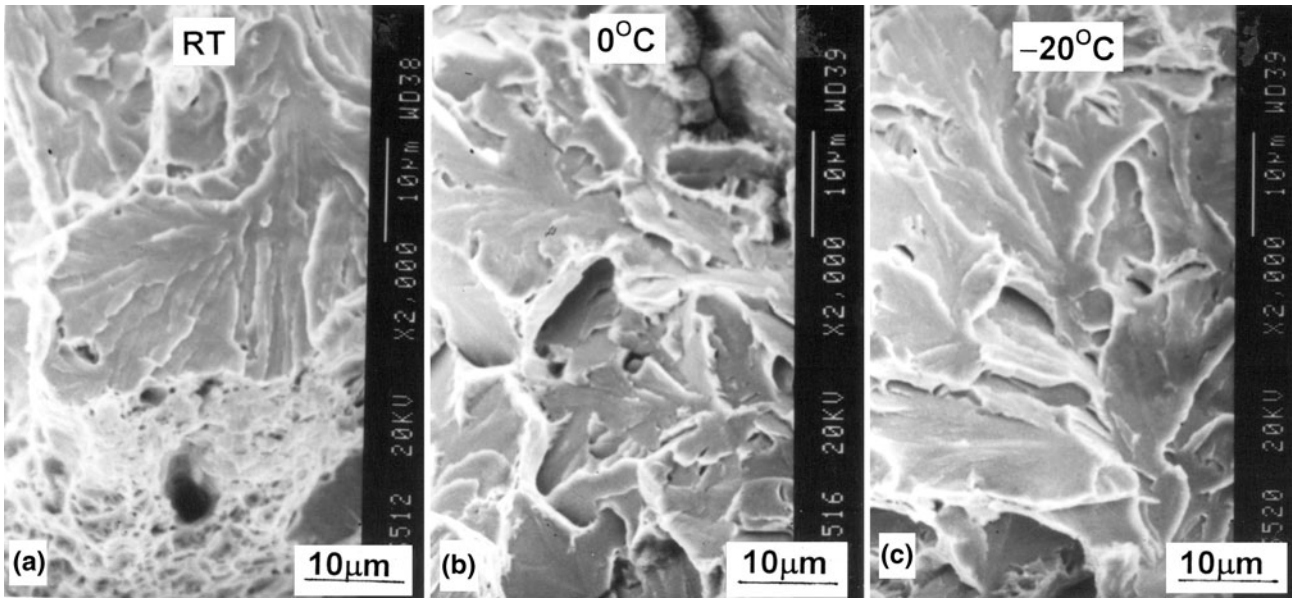

Fig. 20 High-magnification scanning electron fractographs of broken Charpy specimens at (a) RT, (b) 0 °C, and (c) −20 °C

content in the investigated steel was low but adequate for hardenability and tensile properties. The Charpy absorbed energy can be increased, and DBTT lowered by Ni addition as Ni improves the toughness of martensite (Ref 30), and also by refining the austenite grain size in the core by utilizing low Nb additions (Ref 6). This will produce relatively coarse upper bainite and possibly acicular ferrite which is associated with shorter unit crack paths.

Figure 19 shows the low magnification fractographs of Charpy specimens broken at (a) RT, (b) 0°, and (c) −20 °C. Fractographs show increase in lateral contraction at the notch with corresponding decrease of granular region as the temperature rises. High-magnification fractographs (Fig. 20) from the central region of the broken Charpy specimens about 1 mm behind the root of the notch, at RT, 0, and −20 °C, exhibited dimpled to cleavage mixed mode of rupture at RT. The fracture in the specimens tested at 0 °C and −20 °C showed characteristics of a cleavage fracture with facet size increasing upon decreasing the temperature. Presence of small amounts of acicular ferrite in the core region is beneficial for the DBTT, since acicular ferrite has shorter unit crack paths.

4. Conclusions

1. Low Cr additions along with Mn are effective in realizing desired tensile properties of rock bolt steel.
2. Chromium addition increases the hardenability in semi-killed steel in TMT process and produces a microstructure across the bar comprising various transformation products, namely, slightly tempered martensite, lower and upper bainite, and small amounts of acicular ferrite.
3. The presence of coarser upper bainite in association with slightly tempered martensite has no detrimental effect on yield stress, ultimate tensile stress, and elongation. However, it increases the DBTT of the bar and lowers the Charpy absorbed energy due to larger unit crack paths.

Acknowledgments

Thanks are due the management of Steel Authority of India Limited, Bhilai Steel Plant, and Research & Development Center for Iron and Steel, Ranchi, where the work was carried out. Thanks are also due Mr. C.B. Sharma, Mr. A.K. Singh, Mr. B.B. Patra, Mr. John Guria, and Mr. S.N. Hoda for microstructural and tensile tests.

References

1. Standard Specifications for Roof and Rock Bolts and Accessories, ASTM F 432-04, *Annual Book of ASTM Standards*, 2006, **01.08**, p 107-121
2. S. Hashimoto and M. Nakamura, Effect of Microalloying Elements on Mechanical Properties of Reinforcing Bars, *Trans. ISIJ Int.*, 2006, **46**(10), p 1510–1515
3. H. Weise, W. Kramer, W. Bartels, and W.D. Brand, Reinforcing Steel for Reinforced Concrete and Prestressed Concrete Structures, *Steel*, Vol 2, 1st ed., Springer Verlag, New York, 1992, p 61–76
4. A.B. Yure'v, Y.F. Ivanov, V.E. Gromov, and E.V. Kozlov, Structural-Phase State of Thermostrengthened Large Diameter Reinforcement, *Steel Transl.*, 2004, **34**(6), p 69–72
5. B.K. Panigrahi and S.K. Jain, Impact Toughness of High Strength Low Alloy TMT Reinforcement Bar, *Bull. Mater. Sci.*, 2002, **25**(4), p 319–324
6. B.K. Panigrahi, Microstructure-Related Properties of Some Novel Reinforcement Bar Steel, *J. Mater. Eng. Perform.* (online). doi: 10.1007/s11665-009-9456-0
7. B.K. Panigrahi, S. Srikanth, and G. Sahoo, Effect of Alloying Elements on Tensile Properties, Microstructure, and Corrosion Resistance of Reinforcing Bar Steel, *J. Mater. Eng. Perform.* (online). doi: 10.1007/s11665-008-9336-z
8. Y.T. Khudik, A.V. Ivchenko, O.A. Chaikovski, S.A. Madatyan, M.I. Kostyuchenko, and J.N. Surikov, Thermomechanically Strengthened 25 G2S Reinforcing Steel of Strength Class at IVS, *Steel USSR*, 1988, **18**(6), p 272–277
9. V.I. Stolyarov, V.N. Nikiten, L.J. Efron, and V.G. Laz'ko, Status and Outlook of Production Technology for 700 N/mm^2 Yield Strength Weldable Steels, *Steel Transl.*, 1993, **23**(6), p 27–32
10. I.G. Uzlov, Y.T. Khudik, and V.T. Chernenko, Optimisation of Service Properties of Thermomechanically Strengthened Reinforcing Steel, *Steel Transl.*, 1993, **19**(11), p 500–502

11. W. Dahl, Mechanical Properties, *Steel*, Vol 1, 1st ed., Springer Verlag, New York, 1992, p 203–378
12. T.N. Baker, Microalloyed Steels, *Science Progress*, Vol 65, Blackwell Scientific Publisher, Oxford, 1978, p 493–542
13. M. Sarkaya, B.G. Steinberg, and G. Thomas, Optimisation of Fe/Cr/C Base Structural Steel for Improved Strength and Toughness, *Met. Trans.*, 1982, **13A**(12), p 2227–2237
14. W. Pitsch and G. Sauthoff, Typical Microstructures in Steel, *Steel*, Vol 1, 1st ed., Springer Verlag, New York, 1992, p 83
15. H.J. Aaronson, W.T. Reynolds, G.J. Shiflet, and G. Spanos, Bainite Viewed Three Different Ways, *Met. Trans.*, 1990, **21A**(6), p 1343–1380
16. H. Ohtani, S. Okaguchi, Y. Fuzishiro, and Y. Ohmori, Morphology and Properties of Low Carbon Bainite, *Met. Trans.*, 1990, **21A**, p 877–888
17. S. Morooka, Y. Tomota, and T. Kamiyama, Heterogenous Deformation Behavior Studied by In-Situ Neutron Diffraction During Tensile Deformation for Ferrite, Martensite, and Pearlite Steel, *ISIJ Int.*, 2008, **48**(4), p 525–530
18. S. Barnard, G.D.W. Smith, M. Sarikaya, and G. Thomas, Carbon Atom Distribution in a Dual Phase Steel: An Atom Probe Study, *Scr. Metall.*, 1981, **15**(4), p 387–392
19. G.E. Dieter, *Mechanical Metallurgy*, SI Metric Edition, Part 3, Chap. 9, McGraw-Hill Book Co., London, 1988, p 325–337
20. G. Spanos, H.S. Fang, and H.I. Aaronson, A Mechanism for the Formation of Lower Bainite, *Met. Trans.,* 1990, **21A**(6), p 1381–1390
21. R.W.K. Honeycombe and F.B. Pickering, Ferrite and Bainite in Alloy Steels, *Met. Trans.*, 1972, **3**(5), p 1099–1112
22. R.W.K. Honeycombe, *Structure and Strength of Alloy Steels*, Climax Molybdenum Co., London, 1971, p 1–36
23. B.L. Bramfitt and J.G. Speer, A Perspective on the Morphology of Bainite, *Met. Trans.*, 1990, **21A**(4), p 817–829
24. F.B. Pickering, *Physical Metallurgy and Design of Steels*, Chap. 6, 1st ed., Applied Science Publishers, London, 1978
25. D.V. Edmonds and R.C. Cochrane, Structure-Property Relationships in Bainitic Steel, *Met. Trans.*, 1990, **21A**(6), p 1527–1540
26. B. Dogan and J.D. Boyd, Through Thickness Failure of Ti-V-N Steel, *Met. Trans.*, 1990, **21A**(5), p 1177–1191
27. M.L. Joki, V. Vitek, and C.J. McMahon, A Microscopic Theory of Brittle Fracture in Deformable Solids: A Relation Between Ideal Work to Fracture and Plastic Work, *Acta Metall.*, 1980, **28**(11), p 1479–1488
28. D. Kwon and R.J. Asaro, A Study of Void Nucleation, Growth, and Coalescence in Spherodised 1518 Steel, *Met. Trans.*, 1990, **21A**(1), p 117–134
29. W.D. Biggs, Fracture, *Physical Metallurgy,* 2nd revised ed., R.W. Cahn, Ed., North Holland Publishing Co., Amsterdam, 1970, p 1199–1232
30. W.C. Leslie, *The Physical Metallurgy of Steels,* McGraw Hill International Book Co., New York, p 289–300